11.12.2023

Label-free imaging of DNA interactions with 2D materials

Jenny Sülzle[1,*], Wayne Yang[2,*,†], Yuta Shimoda[2], Nathan Ronceray[2], Eveline Mayner[2], Suliana Manley[1,†], and Aleksandra Radenovic[2,†]

[1] Institute of Physics and Institute of Bioengineering, Laboratory of Experimental Biophysics (LEB), École Polytechnique Fédérale de Lausanne (EPFL), Switzerland

[2] Institute of Bioengineering, Laboratory of Nanoscale Biology (LBEN), École Polytechnique Fédérale de Lausanne (EPFL), Switzerland

* Equal contribution

[†] Corresponding authors:

aleksandra.radenovic@epfl.ch; suliana.manley@epfl.ch; wayne.yang@epfl.ch

Abstract:

Two-dimensional (2D) materials offer potential as substrates for biosensing devices, as their properties can be engineered to tune interactions between the surface and biomolecules. Yet, not many methods can measure these interactions in a liquid environment without introducing labeling agents such as fluorophores. In this work, we harness interferometric scattering (iSCAT) microscopy, a label-free imaging technique, to investigate the interactions of single molecules of long dsDNA with 2D materials. The millisecond temporal resolution of iSCAT allows us to capture the transient interactions and to observe the dynamics of unlabeled DNA binding to a hexagonal boron nitride (hBN) surface in solution for extended periods (including a fraction of 10%, of trajectories lasting longer than 110 ms). Using a Focused Ion Beam (FIB) technique to engineer defects, we find that DNA binding affinity is enhanced at defects; when exposed to long lanes, DNA binds preferentially at lane edges. Overall, we demonstrate that iSCAT imaging is a useful tool to study how biomolecules interact with 2D materials, a key component in engineering future biosensors.

Keywords: DNA-surface interactions, interferometric scattering, 2D materials, biosensing

28 Two-dimensional (2D) materials have been developed as DNA sensing platforms owing to
29 their chemical, electronic and mechanical properties which accommodate a variety of sensing
30 modalities such as membrane-embedded nanopores[1–7], tunneling junctions[8,9] and field-effect
31 transistors[10,11]. Such devices have succeeded in sensing individual DNA strands, both optically and
32 electronically[12–16]. Different sensing modalities and functionalisations can be integrated to detect a
33 whole host of biological analytes with a single device, which due to a high surface-to-volume ratio can
34 be performed on limited sample volumes.

35 An important remaining challenge is to control surface interactions and to prevent fouling of
36 the devices[17]. Toward this end, understanding DNA interactions with 2D materials is crucial to improve
37 biosensor designs by reducing unwanted interactions and by promoting desired ones. A common
38 approach is to label DNA fluorescently with intercalating dyes (such as YOYO-1) and study it with
39 optical microscopy[18]. Alternatively, atomic force microscopy (AFM) can simultaneously detect
40 molecular binding and map the surfaces[19,20]. Electron microscopy (EM) has also been used to image
41 2D materials in the presence of biomolecules at even higher spatial resolution[21–23]. However, each of
42 these approaches suffers from limitations. Intercalating dyes change the length and stiffness of
43 DNA[24,25], and such dyes suffer from photobleaching and quenching near 2D material surfaces[26,27]. AFM
44 offers imaging in liquid, but only for hydrophilic substrates such as mica. In the case of prototypical 2D
45 materials, such as graphene, hexagonal boron nitride (hBN) or transition metal dichalcogenides
46 (TMDCs), imaging is often limited to dried DNA on 2D material surfaces. EM is largely confined to dry
47 specimens and thus lacks dynamic information, or requires special liquid holders or the use of gold
48 nanoparticles as labels[28–32]. This may explain in part why simulation has led experiment in investigating
49 interactions of DNA with more complex materials and device designs[33–36].

50 In this work we harness interferometric scattering (iSCAT) microscopy[37,38] to investigate single
51 molecules of long double stranded (ds)DNA interacting with the surface of hBN. As an analyte in
52 solution approaches the surface, interference between the light it scatters and the light reflected by

the liquid-solid interface boosts the signal contrast, enabling single-molecule detection. Because iSCAT uses the molecules themselves to generate signal, it does not require labeling. Liberated from the limited photon budget of fluorescent dyes, the technique allows millisecond temporal resolution, and theoretically indefinite imaging times. So far, iSCAT has been used to study the mass distribution of short single-stranded and double-stranded DNA[39], protein oligomers down to molecular weights of 10 kDa[40,41], and the products of other biomolecular reactions[42] as well as the dynamics of more complex cellular processes[43]. To study the effects of surface properties on DNA binding, we study its interactions with pristine hBN as well as engineered defects and nanostructures[44].

We chose hBN as our substrate due to its optical properties: it is transparent because of its band gap of 6 eV[45], and it uniquely among 2D materials[27,46–48] lacks fluorescence quenching which allows integration with fluorescent sensing strategies. Additionally, we note the potential for future engineering[33] due to its regular shaped crystal edges[49–51] and single layer films which appear promising candidates for high-quality large-scale production[52–54]. hBN was exfoliated on coverslips and imaged with iSCAT (Figure 1a, SI Experimental Section). The hBN flakes show a static uniform scattering background when illuminated in water, with stronger scattering from their edges. To prevent edge scattering from overwhelming the weaker signal from dsDNA, we imaged the larger flakes, and ensured they filled the selected FOV (Figure S1). Furthermore, we use multiple frames to calculate a running averaged scattering background and to produce a differential contrast image.

Upon the addition of DNA, we observe the appearance of large scattering signals (blobs) with bright and dark regions in images following median-filtered background removal (Figure 1b). We measure similar patterns for a range of different DNA lengths: 10, 20, and 48 kbp (Figure S2). These sizes were chosen based on our observed lower detection limit of 10 kbp dsDNA. We expect that the observed blobs of DNA are of single molecules, consistent with observations of both labeled and unlabeled DNA by other single molecule sensing techniques employing similar concentrations (pM-nM) of DNA[55–57].

78 Theoretical and experimental studies have demonstrated that iSCAT is highly sensitive to the
79 axial position of scattering particles, and even nanometric changes can result in a contrast inversion
80 in the temporally-filtered images, due to constructive and destructive interference[58,59]. These studies
81 measured biomolecules much smaller than the diffraction limit, which led to compact, circularly
82 shaped interferometric point spread functions (iPSF). In our case, the estimated radii of gyration for
83 the measured DNA molecules are 238 nm (10 kbp dsDNA), 337 nm (20 kbp) and 521 nm (48 kbp). We
84 speculate that the complex scattering signal is a superposition of multiple iPSFs from different parts
85 of the same molecule, which spans several hundred nanometers axially. Similar studies with iSCAT
86 show a linear correlation of the contrast signal to the molecular mass of the analyte for molecules
87 much smaller than the diffraction limit[39,40,60]. Here, we chose the mean contrast signal of each
88 localization to investigate its relationship to molecular weight, but we did not find a correlation for
89 these large DNA molecules.

90 In time-lapse experiments, we qualitatively observe motion of the scattering blobs (Figure 1b,
91 Figure S3 and Movie S1). The overall signal contrast is typically low in the frames when a particle
92 approaches or leaves the surface, but it increases when particles are moving along the surface. We
93 wished to quantify this motion, but we noticed that the same molecule could change contrast, shape,
94 and size from frame to frame. We speculate that this is due to changing 3D conformations of the
95 dsDNA on the hBN surface. Existing strategies for detection and localization such as thresholding and
96 spot detection yield poor efficiency due to this complex appearance - this motivated us to develop a
97 customized image analysis pipeline.

98 We developed an approach to segment and localize the particles for data with a temporal
99 median-filtered background normalization (Figure 2a, Figure S4, S5, S6). We use the absolute value of
100 the signal, to combine both constructive and destructive interference contributions to the signal. We
101 optimize the threshold to avoid false positives from the noisy background, while still detecting faint
102 signals. Each particle's absolute contrast-weighted center of mass defines its location, which can be

103 connected in time to reconstruct trajectories (SI Experimental Section). We manually validated the
104 automatically-tracked results by checking each step in the pipeline for a randomly selected subset of
105 particles. We define each detected localization as a DNA binding site, and the total time of
106 reconstructed trajectories as dwell time.

107 On pristine hBN, we observe a wide range of trajectory geometries and lengths (Figure 2b).
108 We split them into two groups (Figure 2c): those that are shorter than or equal to 110 ms (523 out of
109 581 total trajectories) and those that are longer than 110 ms (58 out of 581 total trajectories). Overall,
110 the measured mean dwell time for 20 kbp dsDNA on pristine hBN is 51.2 [49.0, 57.4] ms (N= 581
111 trajectories, *Mean [95% confidence interval*). We noticed some particles diffusing out of the measured
112 FOV (3.4 µm x 3.4 µm), which would lead to a slight underestimate of dwell times. The observed
113 dynamic nature of the DNA trajectories suggests that interactions of dsDNA with the hBN surface are
114 transient, allowing molecules to adsorb temporarily on the surface, and diffuse laterally before
115 detaching and diffusing back into the bulk solution.

116 Additionally, we noticed a large proportion of brief interactions; in our dataset we measured
117 554 single-frame binding events, and 581 trajectories that last at least for two frames. Single-frame
118 binding events likely correspond to DNA interacting transiently with the surface due to weak charge-
119 mediated surface interactions. To test this idea, we varied the salt concentration by adding 50 mM of
120 KCl. Under this condition, there appears to be fewer binding events per area and time (Movie S3).
121 Transient binding events, where the DNA molecule diffuses in and out of the imaging volume vs. along
122 the surface, are expected to be short-lived, lasting less than a few milliseconds corresponding to a
123 fraction of a frame. Detecting these events with fluorescence microscopy would be challenging due to
124 their brief duration; however, with iSCAT microscopy, we were able to take advantage of its temporal
125 resolution to capture these events.

126 We hypothesized that it would be possible to influence the DNA binding kinetics by
127 engineering the surface with fabricated structures that host more defects and hence present more

128 binding sites. To test this idea, we turned to a recently developed surface engineering method[44]
129 (Figure 3a, SI Experimental Section). While the technique was first demonstrated to produce optical
130 emitters, we saw two potential advantages for our application: there may be minimal damage to the
131 underlying surface of hBN revealed after the water etching step is completed, and the controlled
132 etching may reduce background scattering of the patterned hBN surfaces and edges. As a
133 demonstration, we patterned an array of craters, and monitored the surface with AFM imaging (Figure
134 3b). The sample was submerged in H_2O to etch away the patterned surface, and within 15 min craters
135 started forming. We continued imaging the sample until the depth of the craters stabilised at ~12 nm
136 after about one hour. We also etched lanes using the same process, 1 µm wide, 35 nm deep, and
137 spaced 1 µm apart (Figure 3c). To characterize our structures, we quantified the RMS roughness of the
138 surface. The RMS roughness along the inner trench area of the lanes is 2 nm, while for a single line
139 scan it is even lower (0.3- 0.5 nm), and of the surrounding hBN flake area is 1.8 nm (Figure S7).

140 To observe the effect of surface modifications on the DNA binding affinity, we performed
141 iSCAT imaging experiments on a single large square FIB-milled onto a flake. Similar FIB milling
142 processes have yielded increased densities of optically active emitters (up to 40x increase, Figure S8)
143 in hBN indicating an increase in defect sites. We reconstructed the trajectories of the DNA on the FIB-
144 milled areas (Figure 4a), and found a mean dwell time of 77.9 [74.8, 86.4] ms (N= 874 trajectories,
145 *Mean [95% confidence interval]*; Figure 4b). This is significantly larger than the dwell time of 51.2 [49.0,
146 57.4] ms on the native flake. This indicates that there is an increased binding affinity, possibly from
147 interactions with the FIB milling induced defects on the hBN flake. The nanoscopic origins and strength
148 of these interactions are still up for debate but a few hypotheses include increased electrostatic
149 interactions[36], hydrogen bonding[61], stacking of the DNA on the hBN[61,62] and reactivity with chemical
150 species along the defect sites[63].

151 Next, we performed iSCAT imaging on hBN patterned with narrow lanes by the same process
152 described above for the square (Figure 4c, Movie S2). The edges of the lanes offered scattering

153 contrast, allowing us to contextualize the binding of 20 kbp DNA to the surface. We observed an
154 accumulation of DNA localizations along the edges of the etched lanes (x axis, Figure 4d, Figure S9).
155 The peaks of the accumulation are located between 200- 400 nm away from the edges, within the
156 trenches. In contrast, along the direction of the lanes (y axis), binding events appear uniformly
157 distributed. We examined whether scattering from the lane edges could lead to an increased contrast
158 signal for localizations at the edges, increasing the probability of detecting events in those regions and
159 therefore give a false impression of enhanced binding. Further analysis of the mean absolute contrast
160 intensity revealed no such differences in contrast of binding events, and ruled out this possibility
161 (Figure S10). We therefore interpret the data to indicate enhanced binding of DNA to the inside of the
162 lanes. We estimate a DNA polymer radius of gyration of approximately 330 nm, consistent with the
163 location of the peaks displaced from the edges of the lanes.

164 We wondered whether the preferential binding to lane edges would lead to anisotropic
165 trajectories, e.g. DNA particles preferentially moving along the lanes. To investigate this, we created
166 polar plots of trajectories (Figure S11), and decomposed mean squared displacement (MSD) and step
167 size distributions – along and perpendicular to the lanes (Figure S12, S13, S14). The polar plots do not
168 show a preferential movement along one axis, including when considering only long trajectories.
169 Similarly, the MSD and step size distributions appeared isotropic.

170 In summary, we present a versatile method based on iSCAT for determining dynamic behavior
171 of DNA on two-dimensional materials, in solution and without labels. We demonstrate that iSCAT can
172 distinguish the binding properties of different interfaces. Additionally, the patterning of 2D material
173 surfaces shows that it is possible to engineer the interaction with dsDNA to create sites with increased
174 interactions. Surprisingly, we did not observe the directed motion of DNA along tracks. This calls for
175 future exploration. Nevertheless, biosensing devices can use engineered interactions to enrich
176 molecules within specific sensing regions[64] such as the nanopore's orifice[65,66], ultimately leading to
177 improved sensitivity in single-molecule sensing[67].

178 The data may contain more information about naked DNA's internal configurations and
179 dynamics. We envision that better control over the background signal and new future analyses
180 incorporating iSCAT PSF modeling or deep-learning[41,68] will give more insights into these aspects. Since
181 we avoid modification to DNA's biophysical properties arising from labeling DNA with dye[48] our
182 method will help to guide the computational modelling of DNA- 2D material interactions[36,66]. Our
183 measurements were performed with a temporal resolution of ~11 ms, but other iSCAT instruments
184 demonstrated a temporal resolution of up 1 MHz[69]. This could help understanding conformational
185 changes in the range of microseconds.

186

187

188

189 **Acknowledgments**

190 W.Y. and A.R. would like to acknowledge funding from SNF grant CRSII5_193740. This work was
191 supported by the National Centre for Competence in Research (NCCR) Chemical Biology (S.M., J.S.).
192 We thank Lucie Navratilova for help and useful discussions on the plasma FIB milling. We acknowledge
193 Michal Macha for the help with pFIB. We thank Kyle Douglass, the EPFL Hub for Image Analysis and
194 Daniel Sage for their help and useful discussions on the image analysis workflow. We thank Nicolas
195 Hundt for access to and support with the script for median-filtered iSCAT image processing.

196 **Supporting information**

197 Experimental section and figures as described in the text (PDF)

198 Supplementary Movie S1: Example of 20 kbp dsDNA on pristine hBN imaged with iSCAT (AVI)

199 Supplementary Movie S2: Example of 20 kbp dsDNA on FIB-milled hBN imaged with iSCAT (AVI)

200 Supplementary Movie S3: Example of 20 kbp dsDNA on pristine hBN in DI water and 50 mM KCl (AVI)

Author contribution

J.S., W.Y., S.M. and A.R. conceived the project and designed experiments. J.S., with assistance of W.Y., performed iSCAT imaging experiments. J.S. implemented the image processing framework and performed data analysis. W.Y. prepared the samples, carried out FIB milling, performed fluorescence imaging with the assistance of Y.S. and N.R. and carried out AFM measurements with assistance from E.M.. J.S., W.Y., S.M. and A.R. designed figures and wrote the manuscript.

References

(1) Merchant, C. A.; Healy, K.; Wanunu, M.; Ray, V.; Peterman, N.; Bartel, J.; Fischbein, M. D.; Venta, K.; Luo, Z.; Johnson, A. T. C.; Drndić, M. DNA Translocation through Graphene Nanopores. *Nano Lett.* **2010**, *10* (8), 2915–2921. https://doi.org/10.1021/nl101046t.

(2) Garaj, S.; Hubbard, W.; Reina, A.; Kong, J.; Branton, D.; Golovchenko, J. A. Graphene as a Subnanometre Trans-Electrode Membrane. *Nature* **2010**, *467* (7312), 190–193. https://doi.org/10.1038/nature09379.

(3) Verschueren, D. V.; Yang, W.; Dekker, C. Lithography-Based Fabrication of Nanopore Arrays in Freestanding SiN and Graphene Membranes. *Nanotechnology* **2018**, *29* (14), 145302. https://doi.org/10.1088/1361-6528/aaabce.

(4) Graf, M.; Lihter, M.; Thakur, M.; Georgiou, V.; Topolancik, J.; Ilic, B. R.; Liu, K.; Feng, J.; Astier, Y.; Radenovic, A. Fabrication and Practical Applications of Molybdenum Disulfide Nanopores. *Nat Protoc* **2019**, *14* (4), 1130–1168. https://doi.org/10.1038/s41596-019-0131-0.

(5) Schneider, G. F.; Kowalczyk, S. W.; Calado, V. E.; Pandraud, G.; Zandbergen, H. W.; Vandersypen, L. M. K.; Dekker, C. DNA Translocation through Graphene Nanopores. *Nano Lett.* **2010**, *10* (8), 3163–3167. https://doi.org/10.1021/nl102069z.

(6) Liu, K.; Pan, C.; Kuhn, A.; Nievergelt, A. P.; Fantner, G. E.; Milenkovic, O.; Radenovic, A. Detecting Topological Variations of DNA at Single-Molecule Level. *Nat Commun* **2019**, *10* (1), 3. https://doi.org/10.1038/s41467-018-07924-1.

(7) Danda, G.; Masih Das, P.; Chou, Y.-C.; Mlack, J. T.; Parkin, W. M.; Naylor, C. H.; Fujisawa, K.; Zhang, T.; Fulton, L. B.; Terrones, M.; Johnson, A. T. C.; Drndić, M. Monolayer WS2 Nanopores for DNA Translocation with Light-Adjustable Sizes. *ACS Nano* **2017**, *11* (2), 1937–1945. https://doi.org/10.1021/acsnano.6b08028.

(8) Caneva, S.; Gehring, P.; García-Suárez, V. M.; García-Fuente, A.; Stefani, D.; Olavarria-Contreras, I. J.; Ferrer, J.; Dekker, C.; van der Zant, H. S. J. Mechanically Controlled Quantum Interference in Graphene Break Junctions. *Nature Nanotech* **2018**, *13* (12), 1126–1131. https://doi.org/10.1038/s41565-018-0258-0.

(9) Huang, S.; He, J.; Chang, S.; Zhang, P.; Liang, F.; Li, S.; Tuchband, M.; Fuhrmann, A.; Ros, R.; Lindsay, S. Identifying Single Bases in a DNA Oligomer with Electron Tunnelling. *Nature Nanotech* **2010**, *5* (12), 868–873. https://doi.org/10.1038/nnano.2010.213.

(10) Heerema, S. J.; Dekker, C. Graphene Nanodevices for DNA Sequencing. *Nature Nanotech* **2016**, *11* (2), 127–136. https://doi.org/10.1038/nnano.2015.307.

(11) Girdhar, A.; Sathe, C.; Schulten, K.; Leburton, J.-P. Graphene Quantum Point Contact Transistor for DNA Sensing. *Proceedings of the National Academy of Sciences* **2013**, *110* (42), 16748–16753. https://doi.org/10.1073/pnas.1308885110.
(12) Yamazaki, H.; Kimura, S.; Tsukahara, M.; Esashika, K.; Saiki, T. Optical Detection of DNA Translocation through Silicon Nanopore by Ultraviolet Light. *Appl. Phys. A* **2014**, *115* (1), 53–56. https://doi.org/10.1007/s00339-013-7956-0.
(13) Soni, G. V.; Singer, A.; Yu, Z.; Sun, Y.; McNally, B.; Meller, A. Synchronous Optical and Electrical Detection of Biomolecules Traversing through Solid-State Nanopores. *Review of Scientific Instruments* **2010**, *81* (1), 014301. https://doi.org/10.1063/1.3277116.
(14) Assad, O. N.; Di Fiori, N.; Squires, A. H.; Meller, A. Two Color DNA Barcode Detection in Photoluminescence Suppressed Silicon Nitride Nanopores. *Nano Lett.* **2015**, *15* (1), 745–752. https://doi.org/10.1021/nl504459c.
(15) Yang, W.; Dekker, C. Single-Molecule Ionic and Optical Sensing with Nanoapertures. In *Single Molecule Sensing Beyond Fluorescence*; Bowen, W., Vollmer, F., Gordon, R., Eds.; Nanostructure Science and Technology; Springer International Publishing: Cham, 2022; pp 367–387. https://doi.org/10.1007/978-3-030-90339-8_12.
(16) Pitchford, W. H.; Kim, H.-J.; Ivanov, A. P.; Kim, H.-M.; Yu, J.-S.; Leatherbarrow, R. J.; Albrecht, T.; Kim, K.-B.; Edel, J. B. Synchronized Optical and Electronic Detection of Biomolecules Using a Low Noise Nanopore Platform. *ACS Nano* **2015**, *9* (2), 1740–1748. https://doi.org/10.1021/nn506572r.
(17) Schneider, G. F.; Xu, Q.; Hage, S.; Luik, S.; Spoor, J. N. H.; Malladi, S.; Zandbergen, H.; Dekker, C. Tailoring the Hydrophobicity of Graphene for Its Use as Nanopores for DNA Translocation. *Nat Commun* **2013**, *4* (1), 2619. https://doi.org/10.1038/ncomms3619.
(18) Lu, C.; Liu, Y.; Ying, Y.; Liu, J. Comparison of MoS2, WS2, and Graphene Oxide for DNA Adsorption and Sensing. *Langmuir* **2017**, *33* (2), 630–637. https://doi.org/10.1021/acs.langmuir.6b04502.
(19) Pyne, A.; Thompson, R.; Leung, C.; Roy, D.; Hoogenboom, B. W. Single-Molecule Reconstruction of Oligonucleotide Secondary Structure by Atomic Force Microscopy. *Small* **2014**, *10* (16), 3257–3261. https://doi.org/10.1002/smll.201400265.
(20) Pyne, A. L. B.; Noy, A.; Main, K. H. S.; Velasco-Berrelleza, V.; Piperakis, M. M.; Mitchenall, L. A.; Cugliandolo, F. M.; Beton, J. G.; Stevenson, C. E. M.; Hoogenboom, B. W.; Bates, A. D.; Maxwell, A.; Harris, S. A. Base-Pair Resolution Analysis of the Effect of Supercoiling on DNA Flexibility and Major Groove Recognition by Triplex-Forming Oligonucleotides. *Nat Commun* **2021**, *12* (1), 1053. https://doi.org/10.1038/s41467-021-21243-y.
(21) Gentile, F.; Moretti, M.; Limongi, T.; Falqui, A.; Bertoni, G.; Scarpellini, A.; Santoriello, S.; Maragliano, L.; Proietti Zaccaria, R.; di Fabrizio, E. Direct Imaging of DNA Fibers: The Visage of Double Helix. *Nano Lett.* **2012**, *12* (12), 6453–6458. https://doi.org/10.1021/nl3039162.
(22) Zellweger, R.; Lopes, M. Dynamic Architecture of Eukaryotic DNA Replication Forks In Vivo, Visualized by Electron Microscopy. In *Genome Instability: Methods and Protocols*; Muzi-Falconi, M., Brown, G. W., Eds.; Methods in Molecular Biology; Springer: New York, NY, 2018; pp 261–294. https://doi.org/10.1007/978-1-4939-7306-4_19.
(23) Cerf, A.; Alava, T.; Barton, R. A.; Craighead, H. G. Transfer-Printing of Single DNA Molecule Arrays on Graphene for High-Resolution Electron Imaging and Analysis. *Nano Lett.* **2011**, *11* (10), 4232–4238. https://doi.org/10.1021/nl202219w.
(24) Günther, K.; Mertig, M.; Seidel, R. Mechanical and Structural Properties of YOYO-1 Complexed DNA. *Nucleic Acids Research* **2010**, *38* (19), 6526–6532. https://doi.org/10.1093/nar/gkq434.
(25) Rocha, M. S.; Ferreira, M. C.; Mesquita, O. N. Transition on the Entropic Elasticity of DNA Induced by Intercalating Molecules. *The Journal of Chemical Physics* **2007**, *127* (10), 105108. https://doi.org/10.1063/1.2768945.

(26) Tan, A. T. L.; Kim, J.; Huang, J.-K.; Li, L.-J.; Huang, J. Seeing Two-Dimensional Sheets on Arbitrary Substrates by Fluorescence Quenching Microscopy. *Small* **2013**, *9* (19), 3253–3258. https://doi.org/10.1002/smll.201300049.
(27) Kasry, A.; Ardakani, A. A.; Tulevski, G. S.; Menges, B.; Copel, M.; Vyklicky, L. Highly Efficient Fluorescence Quenching with Graphene. *J. Phys. Chem. C* **2012**, *116* (4), 2858–2862. https://doi.org/10.1021/jp207972f.
(28) Dunn, G.; Adiga, V. P.; Pham, T.; Bryant, C.; Horton-Bailey, D. J.; Belling, J. N.; LaFrance, B.; Jackson, J. A.; Barzegar, H. R.; Yuk, J. M.; Aloni, S.; Crommie, M. F.; Zettl, A. Graphene-Sealed Flow Cells for In Situ Transmission Electron Microscopy of Liquid Samples. *ACS Nano* **2020**, *14* (8), 9637–9643. https://doi.org/10.1021/acsnano.0c00431.
(29) Yuk, J. M.; Park, J.; Ercius, P.; Kim, K.; Hellebusch, D. J.; Crommie, M. F.; Lee, J. Y.; Zettl, A.; Alivisatos, A. P. High-Resolution EM of Colloidal Nanocrystal Growth Using Graphene Liquid Cells. *Science* **2012**, *336* (6077), 61–64. https://doi.org/10.1126/science.1217654.
(30) de Jonge, N.; Ross, F. M. Electron Microscopy of Specimens in Liquid. *Nature Nanotech* **2011**, *6* (11), 695–704. https://doi.org/10.1038/nnano.2011.161.
(31) Zheng, H.; Claridge, S. A.; Minor, A. M.; Alivisatos, A. P.; Dahmen, U. Nanocrystal Diffusion in a Liquid Thin Film Observed by in Situ Transmission Electron Microscopy. *Nano Lett.* **2009**, *9* (6), 2460–2465. https://doi.org/10.1021/nl9012369.
(32) Chen, Q.; Smith, J. M.; Park, J.; Kim, K.; Ho, D.; Rasool, H. I.; Zettl, A.; Alivisatos, A. P. 3D Motion of DNA-Au Nanoconjugates in Graphene Liquid Cell Electron Microscopy. *Nano Lett.* **2013**, *13* (9), 4556–4561. https://doi.org/10.1021/nl402694n.
(33) Zhang, L.; Wang, X. DNA Sequencing by Hexagonal Boron Nitride Nanopore: A Computational Study. *Nanomaterials* **2016**, *6* (6), 111. https://doi.org/10.3390/nano6060111.
(34) Manzanares-Palenzuela, C. L.; Pourrahimi, A. M.; Gonzalez-Julian, J.; Sofer, Z.; Pykal, M.; Otyepka, M.; Pumera, M. Interaction of Single- and Double-Stranded DNA with Multilayer MXene by Fluorescence Spectroscopy and Molecular Dynamics Simulations. *Chem. Sci.* **2019**, *10* (43), 10010–10017. https://doi.org/10.1039/C9SC03049B.
(35) Chen, S. H.; Bell, D. R.; Luan, B. Understanding Interactions between Biomolecules and Two-Dimensional Nanomaterials Using in Silico Microscopes. *Advanced Drug Delivery Reviews* **2022**, *186*, 114336. https://doi.org/10.1016/j.addr.2022.114336.
(36) Shankla, M.; Aksimentiev, A. Step-Defect Guided Delivery of DNA to a Graphene Nanopore. *Nat. Nanotechnol.* **2019**, *14* (9), 858–865. https://doi.org/10.1038/s41565-019-0514-y.
(37) Lindfors, K.; Kalkbrenner, T.; Stoller, P.; Sandoghdar, V. Detection and Spectroscopy of Gold Nanoparticles Using Supercontinuum White Light Confocal Microscopy. *Phys. Rev. Lett.* **2004**, *93* (3), 037401. https://doi.org/10.1103/PhysRevLett.93.037401.
(38) Jacobsen, V.; Stoller, P.; Brunner, C.; Vogel, V.; Sandoghdar, V. Interferometric Optical Detection and Tracking of Very Small Gold Nanoparticles at a Water-Glass Interface. *Opt. Express* **2006**, *14* (1), 405. https://doi.org/10.1364/OPEX.14.000405.
(39) Li, Y.; Struwe, W. B.; Kukura, P. Single Molecule Mass Photometry of Nucleic Acids. *Nucleic Acids Research* **2020**, *48* (17), e97. https://doi.org/10.1093/nar/gkaa632.
(40) Young, G.; Hundt, N.; Cole, D.; Fineberg, A.; Andrecka, J.; Tyler, A.; Olerinyova, A.; Ansari, A.; Marklund, E. G.; Collier, M. P.; Chandler, S. A.; Tkachenko, O.; Allen, J.; Crispin, M.; Billington, N.; Takagi, Y.; Sellers, J. R.; Eichmann, C.; Selenko, P.; Frey, L.; Riek, R.; Galpin, M. R.; Struwe, W. B.; Benesch, J. L. P.; Kukura, P. Quantitative Mass Imaging of Single Biological Macromolecules. *Science* **2018**, *360* (6387), 423–427. https://doi.org/10.1126/science.aar5839.
(41) Dahmardeh, M.; Mirzaalian Dastjerdi, H.; Mazal, H.; Köstler, H.; Sandoghdar, V. Self-Supervised Machine Learning Pushes the Sensitivity Limit in Label-Free Detection of Single Proteins below 10 kDa. *Nat Methods* **2023**, *20* (3), 442–447. https://doi.org/10.1038/s41592-023-01778-2.
(42) Hundt, N.; Cole, D.; Hantke, M. F.; Miller, J. J.; Struwe, W. B.; Kukura, P. Direct Observation of the Molecular Mechanism Underlying Protein Polymerization. *Science Advances* **2022**, *8* (35), eabm7935. https://doi.org/10.1126/sciadv.abm7935.

(43) Küppers, M.; Albrecht, D.; Kashkanova, A. D.; Lühr, J.; Sandoghdar, V. Confocal Interferometric Scattering Microscopy Reveals 3D Nanoscopic Structure and Dynamics in Live Cells. *Nat Commun* **2023**, *14* (1), 1962. https://doi.org/10.1038/s41467-023-37497-7.
(44) Glushkov, E.; Macha, M.; Räth, E.; Navikas, V.; Ronceray, N.; Cheon, C. Y.; Ahmed, A.; Avsar, A.; Watanabe, K.; Taniguchi, T.; Shorubalko, I.; Kis, A.; Fantner, G.; Radenovic, A. Engineering Optically Active Defects in Hexagonal Boron Nitride Using Focused Ion Beam and Water. *ACS Nano* **2022**, *16* (3), 3695–3703. https://doi.org/10.1021/acsnano.1c07086.
(45) Wickramaratne, D.; Weston, L.; Van de Walle, C. G. Monolayer to Bulk Properties of Hexagonal Boron Nitride. *J. Phys. Chem. C* **2018**, *122* (44), 25524–25529. https://doi.org/10.1021/acs.jpcc.8b09087.
(46) Deng, H.; Yang, X.; Gao, Z. MoS2 Nanosheets as an Effective Fluorescence Quencher for DNA Methyltransferase Activity Detection. *Analyst* **2015**, *140* (9), 3210–3215. https://doi.org/10.1039/C4AN02133A.
(47) Kaminska, I.; Bohlen, J.; Rocchetti, S.; Selbach, F.; Acuna, G. P.; Tinnefeld, P. Distance Dependence of Single-Molecule Energy Transfer to Graphene Measured with DNA Origami Nanopositioners. *Nano Lett.* **2019**, *19* (7), 4257–4262. https://doi.org/10.1021/acs.nanolett.9b00172.
(48) Richter, L.; Szalai, A. M.; Manzanares-Palenzuela, C. L.; Kamińska, I.; Tinnefeld, P. Exploring the Synergies of Single-Molecule Fluorescence and 2D Materials Coupled by DNA. *Advanced Materials* **2023**, *35* (41), 2303152. https://doi.org/10.1002/adma.202303152.
(49) Liu, K.; Lihter, M.; Sarathy, A.; Caneva, S.; Qiu, H.; Deiana, D.; Tileli, V.; Alexander, D. T. L.; Hofmann, S.; Dumcenco, D.; Kis, A.; Leburton, J.-P.; Radenovic, A. Geometrical Effect in 2D Nanopores. *Nano Lett.* **2017**, *17* (7), 4223–4230. https://doi.org/10.1021/acs.nanolett.7b01091.
(50) Dai, C.; Popple, D.; Su, C.; Park, J.-H.; Watanabe, K.; Taniguchi, T.; Kong, J.; Zettl, A. Evolution of Nanopores in Hexagonal Boron Nitride. *Communications Chemistry* **2023**, *6* (1), 108. https://doi.org/10.1038/s42004-023-00899-1.
(51) Gilbert, S. M.; Dunn, G.; Azizi, A.; Pham, T.; Shevitski, B.; Dimitrov, E.; Liu, S.; Aloni, S.; Zettl, A. Fabrication of Subnanometer-Precision Nanopores in Hexagonal Boron Nitride. *Scientific Reports* **2017**, *7* (1), 15096. https://doi.org/10.1038/s41598-017-12684-x.
(52) Caneva, S.; Weatherup, R. S.; Bayer, B. C.; Brennan, B.; Spencer, S. J.; Mingard, K.; Cabrero-Vilatela, A.; Baehtz, C.; Pollard, A. J.; Hofmann, S. Nucleation Control for Large, Single Crystalline Domains of Monolayer Hexagonal Boron Nitride via Si-Doped Fe Catalysts. *Nano Lett.* **2015**, *15* (3), 1867–1875. https://doi.org/10.1021/nl5046632.
(53) Fukamachi, S.; Solís-Fernández, P.; Kawahara, K.; Tanaka, D.; Otake, T.; Lin, Y.-C.; Suenaga, K.; Ago, H. Large-Area Synthesis and Transfer of Multilayer Hexagonal Boron Nitride for Enhanced Graphene Device Arrays. *Nature Electronics* **2023**, *6* (2), 126–136. https://doi.org/10.1038/s41928-022-00911-x.
(54) Liu, S.; He, R.; Ye, Z.; Du, X.; Lin, J.; Jiang, H.; Liu, B.; Edgar, J. H. Large-Scale Growth of High-Quality Hexagonal Boron Nitride Crystals at Atmospheric Pressure from an Fe–Cr Flux. *Crystal Growth & Design* **2017**, *17* (9), 4932–4935. https://doi.org/10.1021/acs.cgd.7b00871.
(55) Bell, N. A. W.; Muthukumar, M.; Keyser, U. F. Translocation Frequency of Double-Stranded DNA through a Solid-State Nanopore. *Phys. Rev. E* **2016**, *93* (2), 022401. https://doi.org/10.1103/PhysRevE.93.022401.
(56) Wanunu, M.; Morrison, W.; Rabin, Y.; Grosberg, A. Y.; Meller, A. Electrostatic Focusing of Unlabelled DNA into Nanoscale Pores Using a Salt Gradient. *Nature Nanotech* **2010**, *5* (2), 160–165. https://doi.org/10.1038/nnano.2009.379.
(57) Lastra, L. S.; Bandara, Y. M. N. D. Y.; Nguyen, M.; Farajpour, N.; Freedman, K. J. On the Origins of Conductive Pulse Sensing inside a Nanopore. *Nat Commun* **2022**, *13* (1), 2186. https://doi.org/10.1038/s41467-022-29758-8.
(58) Mahmoodabadi, R. G.; Taylor, R. W.; Kaller, M.; Spindler, S.; Mazaheri, M.; Kasaian, K.; Sandoghdar, V. Point Spread Function in Interferometric Scattering Microscopy (iSCAT). Part I:

Aberrations in Defocusing and Axial Localization. *Opt. Express, OE* **2020**, *28* (18), 25969–25988. https://doi.org/10.1364/OE.401374.

(59) Dong, J.; Maestre, D.; Conrad-Billroth, C.; Juffmann, T. Fundamental Bounds on the Precision of iSCAT, COBRI and Dark-Field Microscopy for 3D Localization and Mass Photometry. *J. Phys. D: Appl. Phys.* **2021**, *54* (39), 394002. https://doi.org/10.1088/1361-6463/ac0f22.

(60) Heermann, T.; Steiert, F.; Ramm, B.; Hundt, N.; Schwille, P. Mass-Sensitive Particle Tracking to Elucidate the Membrane-Associated MinDE Reaction Cycle. *Nat Methods* **2021**, *18* (10), 1239–1246. https://doi.org/10.1038/s41592-021-01260-x.

(61) Ding, N.; Chen, X.; Wu, C.-M. L.; Li, H. Adsorption of Nucleobase Pairs on Hexagonal Boron Nitride Sheet: Hydrogen Bonding versus Stacking. *Phys. Chem. Chem. Phys.* **2013**, *15* (26), 10767–10776. https://doi.org/10.1039/C3CP50912E.

(62) Lee, J.-H.; Choi, Y.-K.; Kim, H.-J.; Scheicher, R. H.; Cho, J.-H. Physisorption of DNA Nucleobases on H-BN and Graphene: vdW-Corrected DFT Calculations. *J. Phys. Chem. C* **2013**, *117* (26), 13435–13441. https://doi.org/10.1021/jp402403f.

(63) Ronceray, N.; You, Y.; Glushkov, E.; Lihter, M.; Rehl, B.; Chen, T.-H.; Nam, G.-H.; Borza, F.; Watanabe, K.; Taniguchi, T.; Roke, S.; Keerthi, A.; Comtet, J.; Radha, B.; Radenovic, A. Liquid-Activated Quantum Emission from Pristine Hexagonal Boron Nitride for Nanofluidic Sensing. *Nat. Mater.* **2023**, *22* (10), 1236–1242. https://doi.org/10.1038/s41563-023-01658-2.

(64) Dong Hoon Shin; Sung Hyun Kim; Kush Coshic; Kenji Watanabe; Takashi Taniguchi; Gerard Verbiest; Sabina Caneva; Aleksei Aksimentiev; Peter G. Steeneken; Chirlmin Joo. Diffusion of DNA on Atomically Flat 2D Material Surfaces. *bioRxiv* **2023**, 2023.11.01.565159. https://doi.org/10.1101/2023.11.01.565159.

(65) Cao, Z.; Yadav, P.; Barati Farimani, A. Which 2D Material Is Better for DNA Detection: Graphene, MoS2, or MXene? *Nano Lett.* **2022**, *22* (19), 7874–7881. https://doi.org/10.1021/acs.nanolett.2c02603.

(66) Wells, D. B.; Belkin, M.; Comer, J.; Aksimentiev, A. Assessing Graphene Nanopores for Sequencing DNA. *Nano Lett.* **2012**, *12* (8), 4117–4123. https://doi.org/10.1021/nl301655d.

(67) Shin, D. H.; Yang, X.; Caneva, S. Single-Molecule Protein Fingerprinting with Photonic Hexagonal Boron Nitride Nanopores. *Acc. Mater. Res.* **2023**, *4* (4), 307–310. https://doi.org/10.1021/accountsmr.3c00016.

(68) Boyle, M. J.; Goldman, Y. E.; Composto, R. J. Enhancing Nanoparticle Detection in Interferometric Scattering (iSCAT) Microscopy Using a Mask R-CNN. *J. Phys. Chem. B* **2023**, *127* (16), 3737–3745. https://doi.org/10.1021/acs.jpcb.3c00097.

(69) Spindler, S.; Ehrig, J.; König, K.; Nowak, T.; Piliarik, M.; Stein, H. E.; Taylor, R. W.; Garanger, E.; Lecommandoux, S.; Alves, I. D.; Sandoghdar, V. Visualization of Lipids and Proteins at High Spatial and Temporal Resolution via Interferometric Scattering (iSCAT) Microscopy. *J. Phys. D: Appl. Phys.* **2016**, *49* (27), 274002. https://doi.org/10.1088/0022-3727/49/27/274002.

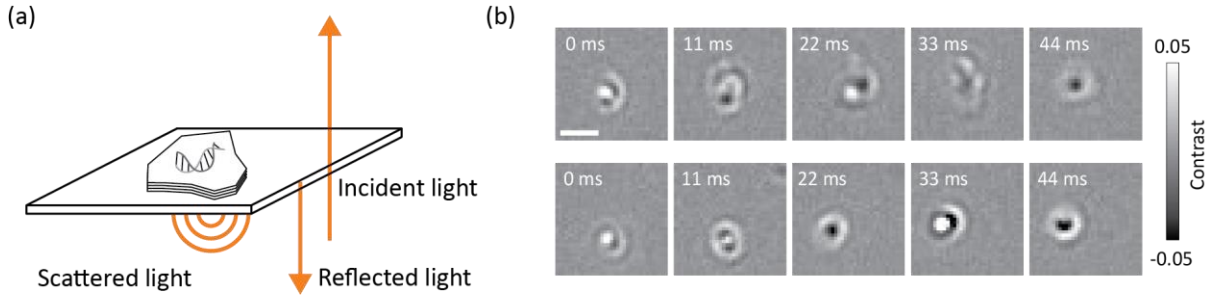

Figure 1. Interaction of 2D materials and DNA probed by iSCAT. (a) Schematic setup of the experiment. (b) Two examples of median-filtered time series of 20 kbp dsDNA particles diffusing on the hBN surface, illustrating changes in shape, size, and contrast of the same molecule from frame-to-frame. Scale bar is 1 µm.

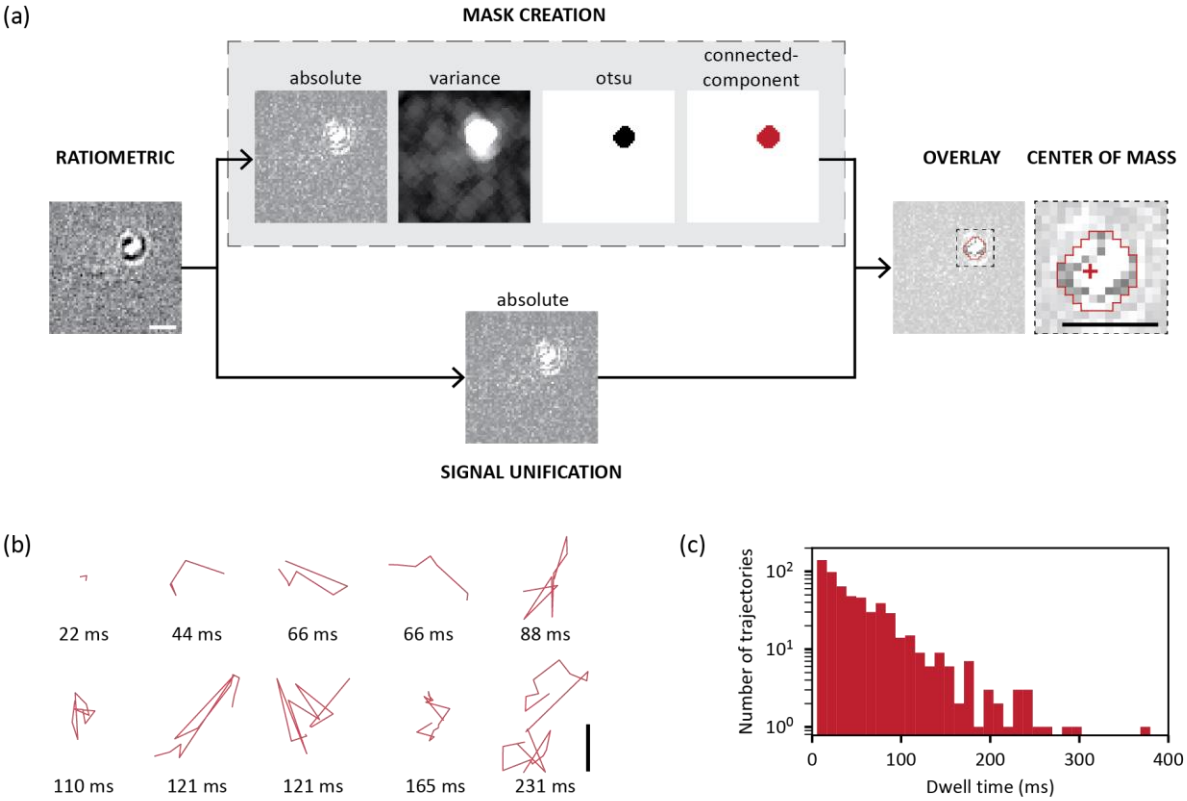

Figure 2. Overview of image processing workflow and of trajectories on pristine hBN. (a) Schematic of image processing workflow. (b) Examples of short and long trajectories on pristine hBN. (c) Dwell time of 20 kbp DNA on pristine hBN. The histogram represents all reconstructed trajectories from three pooled measurement with each 10,000 frames imaged at 90.5 Hz. N (total trajectories) = 581, N (L ≤ 110 ms) = 523, N (L > 110 ms) = 58. Scale bars are 1 μm.

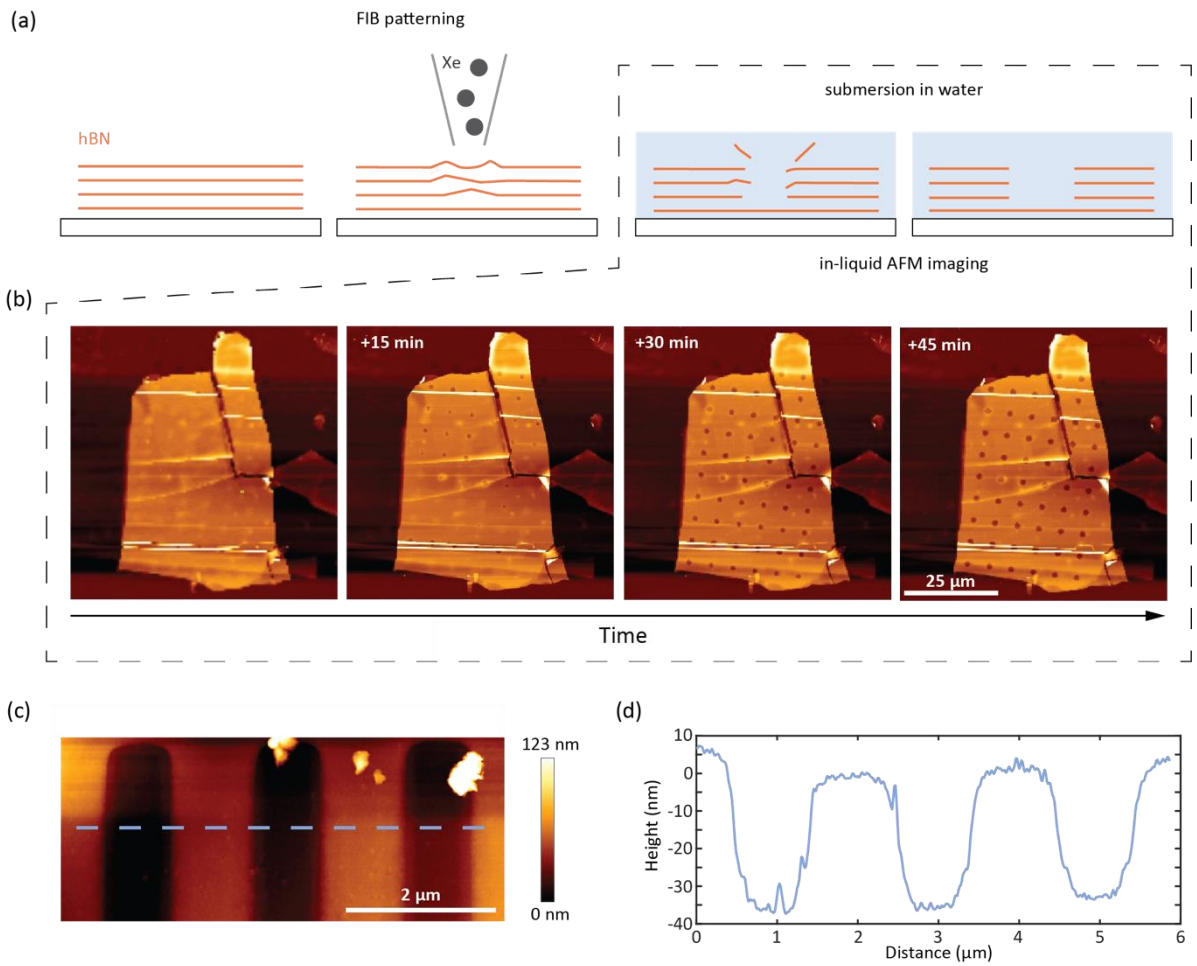

455

456 **Figure 3.** AFM image of pFIB-milled, water-assisted etching of hBN. (a) Illustration of the formation of

457 hBN wells in H_2O. (b) Time series of a dot-patterned hBN flake upon immersion in water. (c) AFM

458 surface map of tracks milled in hBN flake. (d) AFM height profile scan as indicated by the dashed line

459 in (c), RMS roughness along the trench of the lanes is 2 nm.

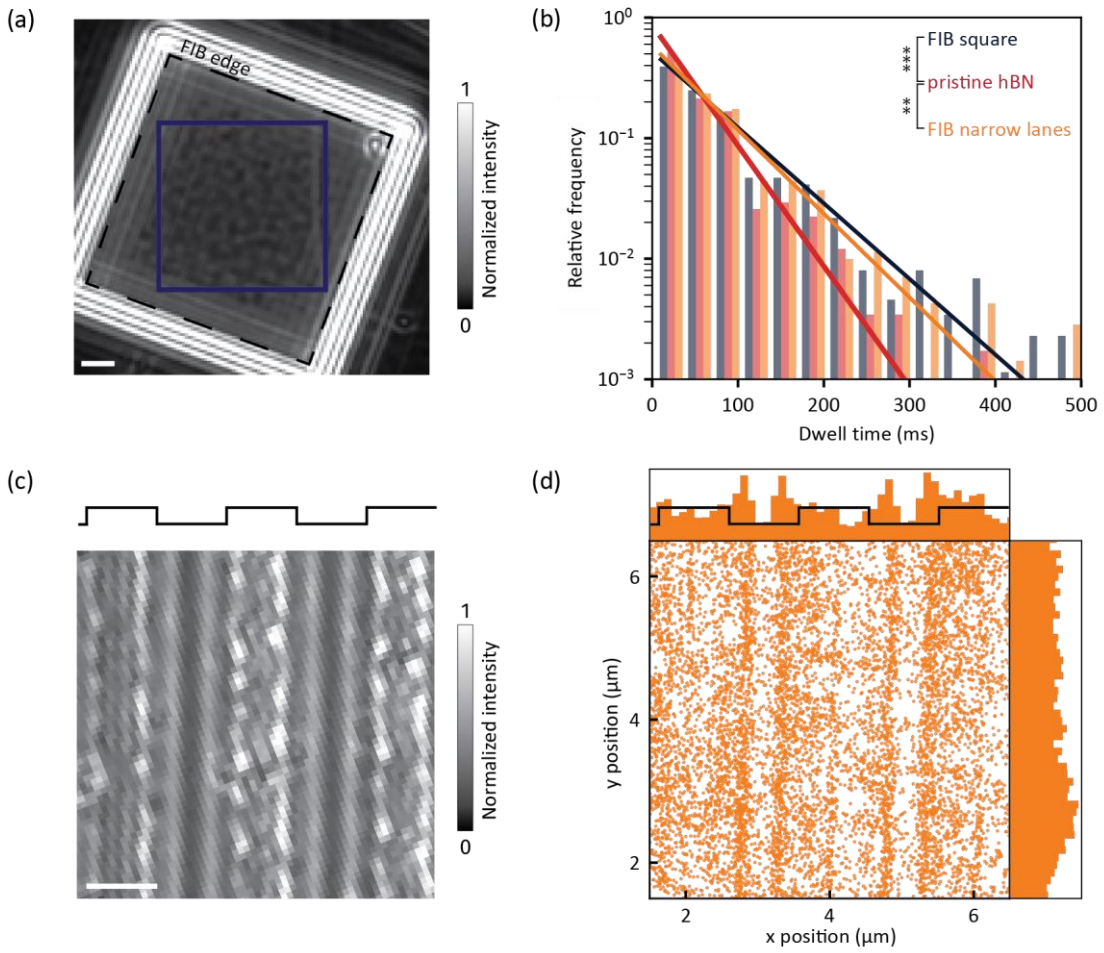

Figure 4. DNA interaction with FIB-milled hBN samples. (a) Native iSCAT image of an hBN flake with an etched square (dashed line). Area used for quantitative analysis is highlighted in blue. (b) Comparison of dwell time of 20 kbp dsDNA on three different surfaces: FIB-etched hBN (FIB square), pristine hBN and hBN patterned with lanes. The histogram represents all reconstructed trajectories from each three pooled measurements. The data was fit to an exponentially decaying distribution. N (FIB square) = 874 trajectories, N (pristine hBN) = 581 and N (FIB lanes) = 703. ****P*-value = 0.000021, ***P*-value = 0.0019. (c) Native iSCAT image of an hBN flake with etched lanes. (d) Distribution of binding spots of 20 kbp dsDNA on sample shown in (c). The scatter histogram represents all localizations from three pooled measurements on the FIB lanes sample shown in (c). N = 9130 localizations. Scale bars are 1 µm.